Classification of projection images of crystalline arrays of the mitochondrial, voltage-dependent anion-selective channel embedded in aurothioglucose

Xiao-Wei Guo and Carmen A. Mannella

Wadsworth Center for Laboratories and Research, New York State Department of Health, Albany, New York 12201-0509 USA; and Departments of Physics and Biomedical Sciences, University at Albany, State University of New York, Albany, New York 12222 USA

ABSTRACT Low-dose electron microscopic images have been recorded from membrane crystals of the mitochondrial, voltage-dependent anion-selective channel, embedded in aurothioglucose. There is considerable variation in the high-resolution detail present in correlation averages computed from these images. Correspondence analysis reveals three classes of "control" averages, with main components of variation involving projected size of the pores and density modulations around the pores and in the corners of the unit cells away from the pores. Pretreatments that affect the functional state of the channel also affect the array averages. In particular, there appears to be a general correlation between the expected effector-induced state (i.e., open and closed) and the projected diameter of the channel lumens in the crystalline arrays.

INTRODUCTION

The mitochondrial outer membrane contains many copies of a voltage-dependent anion-selective channel (VDAC, also called mitochondrial or eukaryotic porin) (1–3). VDAC is very highly conductive at low membrane potentials (4.5 nS in 1 M KCl at 0–10 mV) and switches to lower conducting substates (~2 nS) in the presence of higher membrane potentials or macromolecular effectors (4, 5). By contrast, the "closed" states of VDAC are cation selective and may be impermeable to adenine nucleotides (6).

The ability to generate two-dimensional crystals of this channel, by phospholipase A_2-treatment of fungal outer mitochondrial membranes (7, 8), has made possible structural studies using electron microscopy and image processing (e.g., 9–11). The membrane crystals obtained by this technique are usually collapsed cylindrical tubes, 0.25–0.5 μm wide and 0.5–1.0 μm long, containing several hundred coherent unit cells in each of the two overlapped crystal layers. The small size of these crystals limits the applicability of certain techniques, such as electron diffraction. However, the phospholipase/dialysis preparative method offers several practical advantages over reconstitution procedures and may be expected to be minimally perturbing to protein structure because detergent extraction is not involved. Resolution in correlation averages computed from low-dose projection images of frozen-hydrated VDAC crystals prepared in this way approaches 1.0 nm (12).

There are several polymorphic forms of crystalline VDAC (8, 9, 13), most of which are parallelogram arrays with six transmembrane pores in one unit cell. Each pore is probably formed by a single 31-kD VDAC polypeptide (11, 14). In the most commonly observed array (called "oblique"), there is an angle of 109 ± 1.0° between the **a** and **b** lattice vectors, which are 13.3 and 11.5 nm long, respectively. Lateral phase transitions may occur in the oblique crystals, corresponding (primarily) to sliding of the rows of the array along the **a** direction such that the lattice angle decreases to 99–100°. Interestingly, this contraction of the VDAC lattice can be produced by a synthetic polymer that induces closure of the channel (4, 10). This suggests a possible correlation between the structural states represented by the oblique and contracted polymorphs of crystalline VDAC and functional states of this channel. Other effectors of the VDAC channel are high pH and aluminum (15, 16), both of which tend to inhibit voltage-dependent closure.

Low-resolution three-dimensional reconstructions of the VDAC channel have been computed from tilt-series projections of VDAC arrays embedded in uranyl acetate (17, also C. A. Mannella, unpublished observations). The pore lumens in the unit cell of the oblique arrays span the membrane separately and do not merge into larger openings on one side, as do the channels in the bacterial porin trimer (18). However, the low resolution of these reconstructions (2.5 nm in the crystal plane) severely limits information about the size and shape of the channel lumen. Also, there are concerns that positive staining effects of metal salts may confuse the interpretation of two-dimensional and three-dimensional density maps (9, 19).

We are exploring the use of alternative sugar-based embedding media for obtaining high-resolution (i.e., better than 2 nm) projection images from phospholipase-induced VDAC crystals. Because three-dimensional reconstruction from such radiation-sensitive specimens will require the use of numerous projections from many different crystals, important questions must be answered regarding the reproducibility of images from different crystals. Poor results have been obtained so far with both glucose and tannic acid (20). Resolution in correlation averages of low-dose images of VDAC arrays embedded in either medium at room or liquid-nitrogen temperature does not exceed 2 nm. (This may reflect, in

Address correspondence to Carmen A. Mannella, Wadsworth Center for Laboratories and Research, New York State Department of Health, Empire State Plaza, Box 509, Albany, NY 12201-0509.

0006-3495/92/08/418/10 $2.00

part, difficulties in correcting for lattice disorder in very low contrast images with correlation techniques.) Another embedding medium being tried is aurothioglucose, a molecule of glucose containing a single covalently bound gold atom (10, 21). Like other sugars, aurothioglucose should preserve biological structure well, with the numerous hydroxyl groups on the glucose moiety providing a water-like environment for membrane proteins and lipids. At the same time, the single gold atom in the aurothioglucose molecule provides contrast intermediate between that of heavy-metal salts and metal-free sugars.

The work presented in this report examines the usefulness of aurothioglucose embedding for obtaining reproducible high-resolution images of membrane crystals of the VDAC channel. A set of axial projection images of oblique VDAC arrays has been obtained with resolution better than 2.0 nm and subjected to multivariate statistical analysis to determine the nature of systematic variations in the images.

MATERIALS AND METHODS

Membrane crystal preparation

Outer membranes were isolated from mitochondria of the fungus *Neurospora crassa* (FGSC 326) by hypoosmotic lysis and sucrose gradient centrifugation (22). Crystallization of the VDAC channel protein in the plane of these membranes was carried out by the phospholipase A_2/dialysis technique first described by Mannella (7). Sucrose gradient fractions containing freshly isolated mitochondrial outer membranes were pooled and diluted to ~5 μg protein/ml. Bee-venom phospholipase A_2 (Sigma Chemical Co., St. Louis, MO) was added to the diluted mitochondrial outer membranes at final concentrations of 0.2–2 units/ml. These membrane fractions were then dialyzed against a large volume of low-salt buffer (10 mM tris(hydroxymethyl)-aminomethane-HCl, 1 mM sodium ethylenediaminetetraacetate, pH 7.0) in the cold for 18 h. Afterward, the membranes were centrifuged at 19,000 rpm for 60 min in a SW28 rotor (Beckman Instruments, Inc., Palo Alto, CA) and resuspended in a small volume of low-salt buffer to a final protein concentration of ~0.2 mg/ml.

Electron microscopy: specimen preparation and image recording

In general, specimens were prepared for electron microscopic examination by depositing small (5–10 μl) aliquots of membrane suspension on freshly glow-discharged, carbon-coated, 400-mesh specimen grids. After 2 min, the grids were blotted with filter paper, washed with low-salt buffer containing 1 or 2% aurothioglucose (Sigma Chemical Co.), and air dried. For some specimens, the membranes were suspended in effector-containing buffers before embedding in aurothioglucose. These pretreatments included (*a*) low-salt buffer containing 5 μM of the polyanionic effector, poly-(methacrylate, maleate, styrene), pH 7.0, for 20 or 60 min; (*b*) low-salt buffer containing 50 μM $AlCl_3$, pH 7.0, for 60 min; and (*c*) low-salt buffer, pH 10, for 60 min. The polyanion was a generous gift of T. König (Semmelweis University Medical School, Budapest, Hungary) and M. Colombini (University of Maryland, College Park, MD).

All specimens were examined using an electron microscope (model EM420-T; Philips Electronic Instruments, Inc., Mahwah, NJ) operated at an accelerating voltage of 100 kV. Images were recorded on film (SO163; Eastman Kodak Co., Rochester, NY) at instrument magnification 36,000, using exposures of 0.5–1 s with objective aperture of 50 μm and objective lens defocus of −150 to −300 nm. A low-dose unit (model 6587; Philips Electronic Instruments, Inc.) was used that allows focusing and astigmatism corrections to be made on fields adjacent to those being recorded. Because of the high percentage of tubular VDAC arrays in the membrane preparations used, specimen fields could be recorded "blind," i.e., with no preirradiation. Film developing conditions were used that permitted image recording at a total dose of ~20 electrons/Å^2 (9).

Image processing

Micrographs of well-ordered VDAC arrays were selected by laser diffraction, and crystalline areas were digitized with a flatbed scanning microdensitometer (PDS 1010A; Perkin-Elmer Corp., Garden Grove, CA). A 16.7-μm-square scanning aperture was used, corresponding to a sampling distance of 0.47 nm. Processing of digitized images of VDAC arrays was done with the SPIDER system (23) implemented on graphics workstations (VAXstations 3500 and 3100; Digital Equipment Corp., Marlboro, MA). Projections of individual layers in the collapsed cylindrical membrane crystals were averaged by a procedure (9) that uses quasioptical Fourier-filtration (24) to compute a preliminary average, which is subsequently used as a reference for correlation analysis (25–27).

A subfield (linear dimensions 256 × 256 or smaller) of an array image is padded into a 512 × 512 square field and its Fourier transform computed. An interactive procedure is used to select reflections associated with the reciprocal lattice of one crystal layer in the computed diffraction pattern (Fourier power spectrum; see Fig. 1 *B*). This lattice is refined and used to construct a mask that passes only those Fourier coefficients that fall on the lattice. Inverse transformation of the masked transform yields an average projection of the respective layer of the channel array. A 64 × 64 area is selected from the Fourier-filtered crystal layer, containing a centered hexameric repeating unit surrounded by about one-half unit cell in each direction (see Fig. 1). This reference is cross-correlated with the entire unfiltered field, after padding both reference and image into a $2^n \times 2^n$ matrix, where 2^n is greater or equal to the larger dimension of the unfiltered field. The resulting cross-correlation function contains maxima at locations in the raw image where there is a strong match with the reference. A peak-search program is applied to the cross-correlation function to determine the precise coordinates of the centers of the maxima (28), which in turn are stored in a data file in order of peak height. A map of these peak positions is computed and displayed, and obviously off-lattice points are identified and removed from the "peak coordinate" file by an interactive procedure. The final "correlation average" is formed by addition of 64 × 64 areas extracted from the raw image at the exact positions specified by the revised peak coordinate file, using bilinear interpolation.

To compare projections from different membrane crystals, the correlation averages are aligned by the following procedures. First, the linear dimensions of each square average are increased (to improve alignment precision and correct for slight differences in magnification) by bilinear interpolation to $128(a^*/a^*_{ref})$, where a^*_{ref} is the reciprocal lattice dimension of the image in the set with the largest **a** vector. (Actual deviations in refined lattice parameters of the crystals included in the data set were slight: b^*/a^*, 1.138 ± 0.026; γ, 109.1 ± 1.2°.) After windowing each average to 128 × 128, one of the two possible choices of lattice handedness is selected as reference, and those averages not corresponding to that hand are mirrored. Next, each correlation average is centered on the diad axis at the middle of the channel hexamer, which is located precisely by cross-correlating the average with itself after 180° rotation. Each average is then added to its 180°-rotated version to enforce p2 symmetry. Finally, the averages are rotationally aligned using autocorrelation functions (29). In the first alignment cycle, a member of the data set is used as reference. An average is then made of the aligned data set and is used as a reference for a second

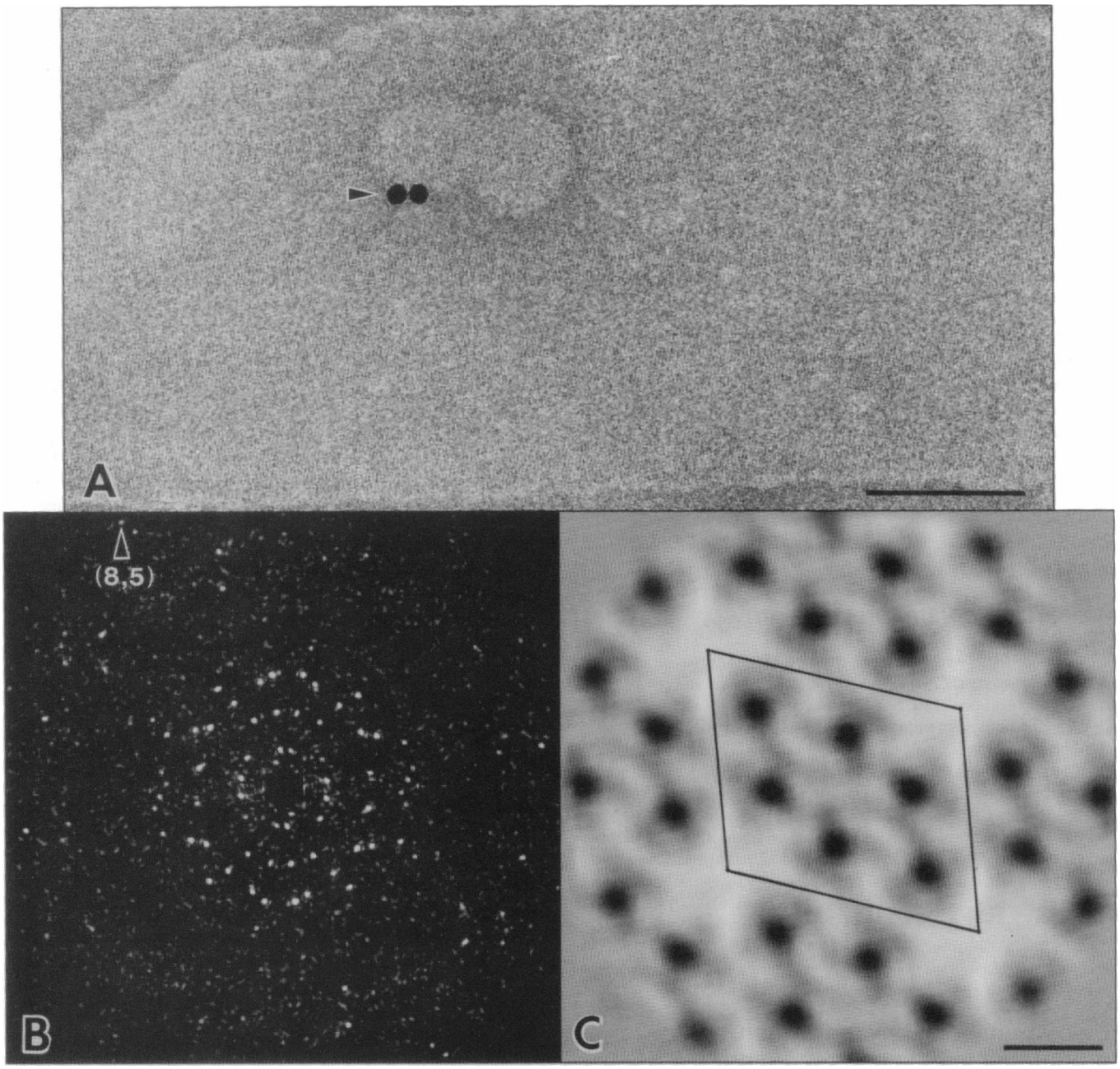

FIGURE 1 (*A*) Electron micrograph of an aurothioglucose-embedded mitochondrial outer membrane containing an "oblique" crystalline array of the VDAC channel. Arrow points to colloidal gold particles that were included as focusing aids in some specimens. Bar, 0.1 μm. (*B*) Computed diffraction pattern of a 120-nm-square region at the center of the membrane in *A*. The reflection indicated by the arrow occurs at 1/(1.67 nm). (*C*) Correlation average of one crystal layer in the membrane of *A* computed over 500 unit cells. The central unit cell is outlined. Bar, 5 nm.

alignment cycle. (The alignment process usually converges after this second cycle.)

Correspondence analysis, a form of multivariate statistical analysis, was used to determine the systematic differences among different correlation averages of the aurothioglucose-embedded VDAC arrays (9, 30). Briefly, an image (correlation average), consisting of p pixels after masking, is represented as a p-dimensional vector whose length in each ith dimension is proportional to the optical density of the ith pixel. The set of aligned images thus forms a "cloud" of points defined in p-space by these vectors. Correspondence analysis determines the orthogonal directions (factor axes) in p-space along which variance in the "image cloud" is greatest.

RESULTS

Averaged projection images of aurothioglucose-embedded membrane crystals

As noted in the Introduction, it was found that low-dose images could be recorded from aurothioglucose-embedded membrane crystals of VDAC that yield correlation averages whose resolution surpasses that achieved either

with conventional negative stains or with glucose or tannic acid. As expected, contrast in these images is intermediate between that of images of membranes embedded in metal salts and in metal-free sugars. Maxima in Fourier power spectra of typical best correlation averages of aurothioglucose-embedded arrays extend out to 1/(1.3 nm), whereas the limit is about 1/(2.0 nm) for arrays embedded in uranyl acetate (9) and in glucose or tannic acid (20). (Correlation averages of unstained frozen-hydrated membrane arrays [12] also may have resolution better than 1/(2.0 nm), but such images are obtained at a much lower frequency than with aurothioglucose embedding.) Fig. 1 *A* is an electron micrograph of a phospholipase A_2-treated aurothioglucose-embedded mitochondrial outer membrane containing two overlapped oblique VDAC arrays. The diffraction pattern (Fourier power spectrum) computed from a 120-nm-square field near the center of this image is presented in Fig. 1 *B*. Reflections from both crystalline layers of the folded vesicle are readily detectable in this pattern past 1/(1.7 nm). Fig. 1 *C* is a correlation average computed from >500 unit cells in one of the crystalline layers in the membrane of Fig. 1 *A*.

The unit cell in the oblique VDAC array contains six dark (aurothioglucose-filled) channel lumens arranged in a hexameric group with a central diad axis. These lumens are the only feature routinely seen in averaged projections of conventionally negatively stained VDAC arrays (9). By contrast, the correlation average of Fig. 1 *C* contains considerable detail (density modulations) outside of the six dark lumens. To determine the reproducibility of the detail in projection images from different crystals, a set of 45 correlation averages (selected from hundreds of images of aurothioglucose-embedded VDAC crystals) was subjected to multivariate statistical analysis (30). Criteria for selection of this data set included consistent image defocus (−150 to −300 nm), detectable maxima in Fourier power spectra of the correlation averages past 1/(1.7 nm), and lattice parameters close to the norm for oblique arrays ($\mathbf{a}$ = 13.3 nm; $\mathbf{b}$ = 11.5 nm; γ = 109°; see Materials and Methods). Most of the correlation averages included in the data set were computed from images of membrane crystals embedded under control conditions (i.e., 1 or 2% aurothioglucose, pH 7.0, no pretreatment). Other averages were computed from images of membrane crystals pretreated with effectors of the channel (as described in Materials and Methods). Pretreatments included incubation with a synthetic amphiphilic polyanion that causes VDAC to close at lower transmembrane potentials (4) and incubation with an aluminum salt and exposure to elevated pH, two conditions that inhibit voltage-dependent closure of the channel (15, 16).

Fig. 2 is a gallery of the 45 correlation averages (computed and aligned by the techniques described in Materials and Methods) of oblique VDAC arrays included in this analysis. The legend to this figure indicates the experimental conditions corresponding to each average. Even a cursory look at this figure indicates considerable variation among the different image averages. Compare, for example, the sizes of the dark (gold-filled) pore lumens in the different averages. The projected diameters of averages 27 and 28 are much larger than those of averages 1 and 3. Also, averages 9 and 43 have significant densities at the corners between the unit cells but not averages 1 and 3.

Correspondence analysis

To detect systematic trends in the observed variations in these image averages, the data set was subjected to correspondence analysis (30). First, the mask shown in Fig. 3 was applied to the averages. The mask encloses a circular area (with a short Gaussian fall-off) containing one unit cell (with 6 channels) and eight nearest-neighbor channels. In addition, the nearest-neighbor channels themselves are excluded by the masks. This was done so that the subsequent analysis might ignore small displacements of the nearest-neighbor channels (expected to arise from the observed small deviations in lattice parameters among the averages in the data set) but still include the corner regions between the unit cells (which appeared to be a site of density variation). The image averages were then scaled (minimum density 0, average density 1) and subjected to correspondence analysis. (Other scaling criteria were also used [30, 31] but did not substantively change the results described below.)

A histogram of the interimage variance associated with the first eight eigenvectors derived from correspondence analysis of the set of 45 image averages is shown in Fig. 4. Factors 1 and 2 account for 24 and 15%, respectively, of the total interimage variance. These first two factors stand out above the next six, which individually include only 7–4% of the total variance. The large portion of the total interimage variance represented by factors 1 and 2 (almost 40%) indicates that they describe much of the systematic variation among the image averages. Therefore, the image cloud was projected onto the plane defined by these factors. This two-dimensional projection map is provided in Fig. 5, in which the position of each of the 45 image averages is indicated by its number in Fig. 2. The experimental conditions used to pretreat arrays are indicated by symbols around the image numbers, as explained in Fig. 5. At the end of each factor axis in the projection map is an "importance image," which illustrates the components of variance represented by that direction in image space. The first (most significant) factor primarily involves the size of the accumulations of aurothioglucose at the lumens of the six channels in the central unit cell. (Arrays with wider pores fall on the left side of the map and those with narrower pores fall on the right side.) The second factor of correspondence analysis has two components: first, the presence (bottom) or ab-

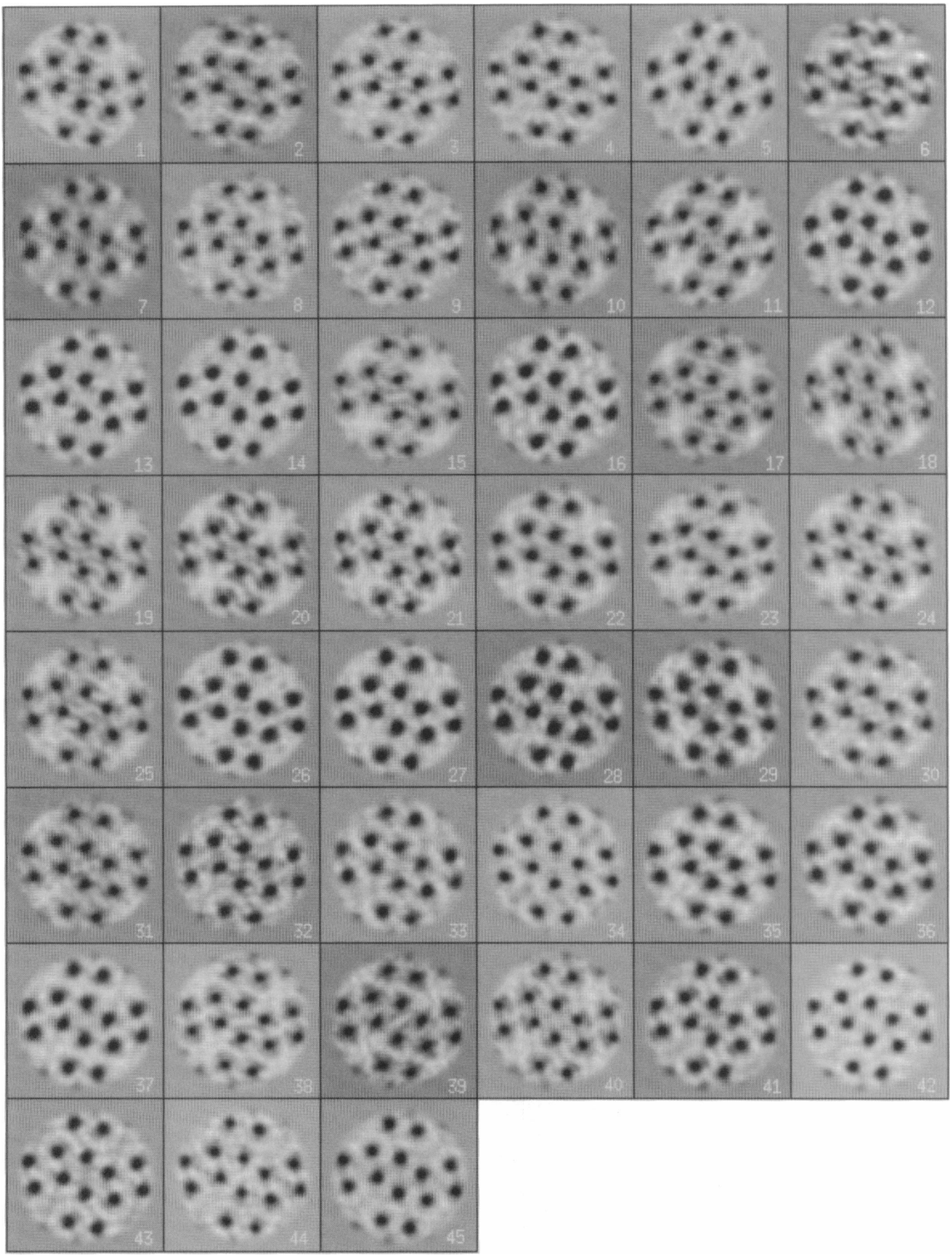

FIGURE 2 Correlation averages of aurothioglucose-embedded "oblique" arrays of VDAC: (1–30) "control" arrays, (31–34) arrays pretreated with the modulator polyanion, (35–40) arrays pretreated with aluminum chloride, (41–45) arrays pretreated at pH 10.

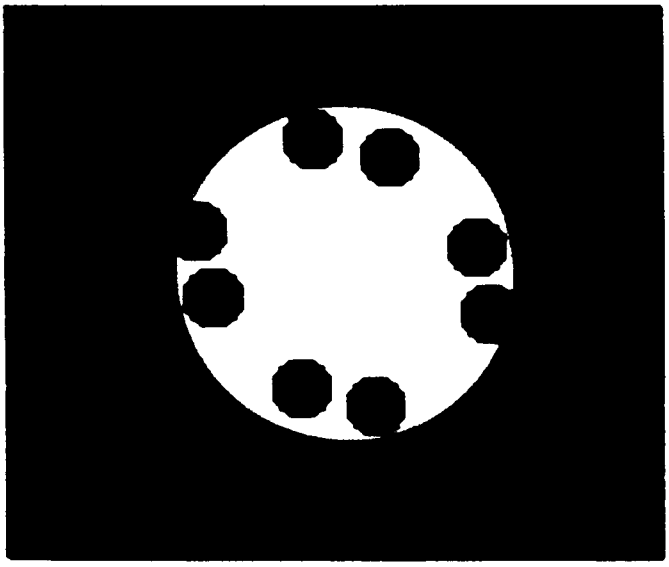

FIGURE 3 Mask applied to the image averages of Fig. 2 before correspondence analysis.

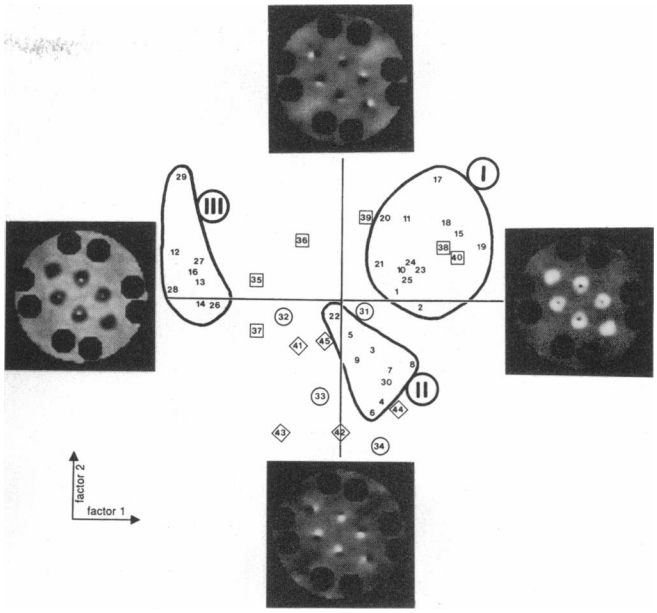

FIGURE 5 Projection map of the image set onto the plane defined by factors 1 and 2 of correspondence analysis. The array positions are indicated by the numbers used in Fig. 2. Numbers corresponding to arrays pretreated before embedding are enclosed by symbols: circles, polyanion pretreated; squares, aluminum pretreated; diamonds, pH 10 pretreated. The three "control" clusters or classes are outlined and labeled I, II, and III. The images at the end of each of the axes are the respective "importance images" (see text).

sence (top) of density at the corners of the unit cells and second, a slight displacement or shift of the centers of the pores within the unit cell (indicated by the adjacent density maximum and minimum at each pore position in the importance images). Importance images of the higher order factors from this analysis were also examined. In general, these factors are more complex than the first two, primarily involving small differences in the positions of various combinations of pores within the unit cell. Projection of the image set along axes of the low-significance factors does not reveal any systematic clustering (unlike results with the first 2 axes; see below), and so these factors are not analyzed further in this report.

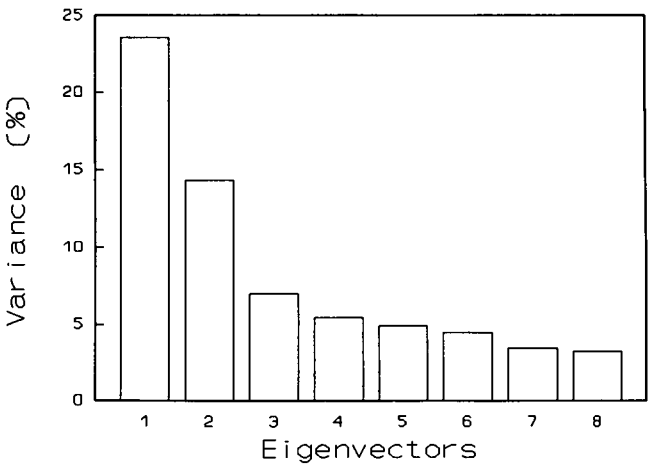

FIGURE 4 Histogram of the interimage variance associated with each eigenvector in correspondence analysis of the 45 correlation averages in Fig. 2.

Classes of control image averages

The image averages of the 30 control VDAC arrays fall into three clusters or classes (labeled I, II, and III in Fig. 5) on the factor 1 vs. factor 2 projection map. Cluster averages, formed by adding control averages in each of the three clusters in this map, are presented in Fig. 6 *A–C*. Cluster averages I and III, which fall on opposite sides of the first factor axis, differ greatly in mean projected diameter of the aurothioglucose accumulation at the pores (~1.4 vs. 2.2 nm). Both cluster averages also display subsidiary density modulations outside the aurothioglucose-filled pores. Several of the densities immediately adjacent to the pore lumens are present in both cluster averages I and III. In addition, cluster average III has "arms" of moderate density extending into the corner regions between the channel hexamers in the oblique array. (These features are also present in the importance images at either end of the first factor axis in Fig. 5.) The diameters of the projected pore lumens in cluster average II are ~1.7 nm, intermediate between those of cluster averages I and III (consistent with the intermediate location of cluster II along factor axis 1). Cluster average II contains density modulations on the periphery of the pore lumens that are more similar to those of cluster average I than cluster average III and additional dense features at the corners of the unit cells not seen in either cluster average I or III.

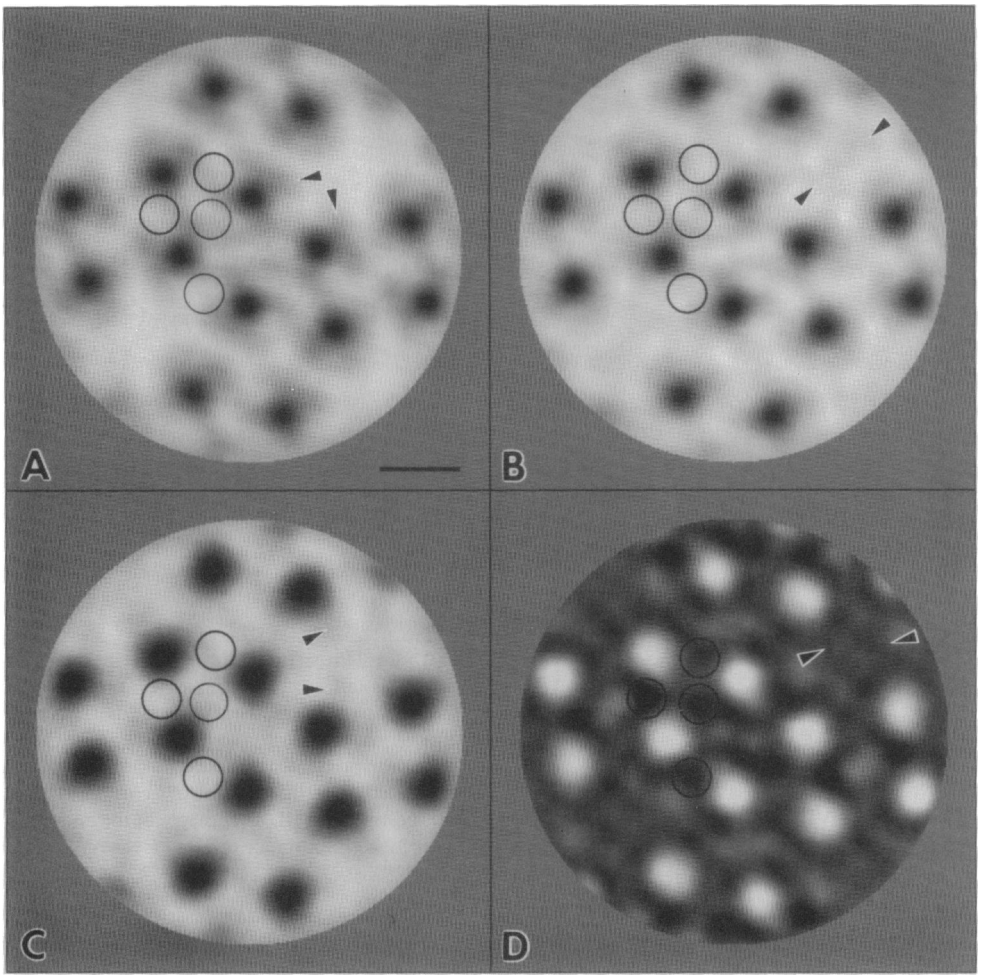

FIGURE 6 Cluster or class averages of "control" VDAC arrays. (*A*) Class I aurothioglucose-embedded array average, with two of the prominent dense features around the pore lumens indicated by arrowheads. (*B*) Class II array average, with characteristic densities at the corners of the unit cell indicated by arrowheads. (*C*) Class III array average. (*D*) Correlation average of a frozen-hydrated unstained VDAC array. The lateral interhexamer "arms" are indicated by arrowheads in *C* and *D*. The circles in *A–D* enclose sites that are low density in *A–C* and high density in *D*. Bar, 10 nm.

Influence of channel effectors on array averages

In addition to 30 control image averages, the data set used for correspondence analysis includes another 15 averages of aurothioglucose-embedded arrays that had been pretreated with effectors of the VDAC channel, namely a synthetic amphiphilic polyanion, aluminum, and high pH. The general effect of the pretreatments is to cause averages of oblique arrays to fall outside the control clusters, although none of the effector-treated arrays fall outside the limits of the projection map defined by the control arrays. (In addition, two of the pretreatments cause changes in the packing geometry of the channels in the arrays. The polyanion induces lattice contraction [10], whereas aluminum causes disordering of the arrays [20]. Only correlation averages of well-ordered oblique arrays are included in the present analysis.)

Seven image averages are included from a previously reported experiment with a polyanionic modulator of the channel (10). The control arrays from this experiment (26–28 in Fig. 2) fall in cluster III, whereas the "+polyanion" arrays (31–34) fall around cluster II. Thus, it appears that the polyanion favors smaller pore lumens and more density in the corners of the unit cell (see Discussion). Eleven of the image averages in the full data set come from two different experiments in which VDAC membrane crystals were incubated with aluminum chloride. Four of the five control arrays (21–25) fall in cluster I, whereas only two of the six "+aluminum" arrays (35–40) fall in cluster I. The other four +aluminum arrays are spread out between clusters I and III on the upper half of the projection map. Finally, six of the image averages in the data set are from an experiment in which VDAC membrane crystals were incubated at pH 10 before embedding. The high pH arrays (41–45) fall near cluster II, which contains a control array from this experiment (30). Four of the five high pH arrays lie farther to the left (big pore) side of the first factor axis than eight of the nine control arrays in cluster II.

DISCUSSION

Interpretation of images of control VDAC arrays

There is considerable variation among projection images obtained from VDAC arrays embedded in aurothioglucose. Correspondence analysis reveals three classes of control image averages, with main components of variation involving projected size of the pores and density modulations around the pores and in the corners of the unit cells away from the channel hexamers. No correlation could be found between the distance of the arrays along either factor axis 1 or 2 in the map of Fig. 5 and slight differences in lattice parameters. Array distribution also does not depend on either handedness (i.e., whether the array corresponds to the top or bottom layer of a collapsed crystalline vesicle) or initial concentration of aurothioglucose (1 or 2%). Therefore, it seems unlikely that the image variations may be associated with variable embedding of the membranes in aurothioglucose. Instead, the observed clustering of the array averages is found to correlate strongly with membrane crystal preparation, i.e., control specimens prepared on a certain day tend to fall into the same cluster or class. The occurrence of different classes of control averages of VDAC crystals may indicate actual preparation-dependent structural differences in the crystals, the underlying causes of which are not now understood.

Some insight into interpretation of correlation averages of control aurothioglucose-embedded VDAC arrays is provided by comparison with the correlation average of an unstained frozen-hydrated array (Fig. 6 *D*) (12). This image average corresponds to a map of the projected density of crystalline VDAC, i.e., low-density regions (water and lipid) are white and protein is dark. The most obvious difference between the aurothioglucose- and vitreous-ice-embedded arrays occurs at the pore lumens, which are dark (gold-filled) in Fig. 6 *A–C* and white (water-filled) in Fig. 6 *D*. Aurothioglucose cluster average III (Fig. 6 *C*) shows the closest overall similarity with the frozen-hydrated array (Fig. 6 *D*); in particular, in terms of pore size and the occurrence of "arms" of moderate density in the regions between the channel hexamers. By contrast, cluster average I has minimum density in the interhexamer regions, whereas cluster average II displays a more centrally located weak density in the same regions. A striking difference between the three aurothioglucose averages and that of the ice-embedded array occurs on the periphery of the pores, i.e., strong density maxima between adjacent pores in Fig. 6 *D* correspond to density minima in Fig. 6 *A–C*. (These positions are circled in Fig. 6.) This systematic difference is consistent with the occurrence of protein protrusions at these positions on the array's surface. Such features would be density maxima in images of unstained arrays but would exclude aurothioglucose and so have minimum density in images of aurothioglucose-embedded arrays.

It appears from the preceding analysis that more than one contrast mechanism is at work in forming high-resolution images of aurothioglucose-embedded arrays. In some ways, aurothioglucose behaves as a negative stain, being accumulated in the pore lumens and excluded by probable surface protrusions. At the same time, the similarity between the dense arms in the class III and frozen-hydrated averages is suggestive of positive contrast. The apparent mixing of negative and positive contrast mechanisms, also noted in an earlier study of aurothioglucose-embedded bacterial surface layers (32), renders high-resolution images of specimens embedded in aurothioglucose (and other low-contrast sugar-metal mixtures) difficult to interpret generally. Unambiguous interpretation of the two-dimensional averages in Fig. 6 *A–C* will require three-dimensional reconstruction of both aurothioglucose- and ice-embedded VDAC arrays (research in progress).

Interpretation of images of effector-treated VDAC arrays

At first glance, the distribution of effector-pretreated arrays in the correspondence analysis map of Fig. 5 appears somewhat random. However, because of the above-noted preparation dependence of the array averages, effector-treated arrays should be compared with control arrays from the same experiment. When this is done, interesting trends are found. The polyanion that induces channel closure "moves" the arrays from cluster III to the right along factor axis 1, in the direction of small pore size. By contrast, the two pretreatments that inhibit pore closure (aluminum and high pH) cause the arrays to distribute to the left of their respective control images along the first factor axis, in the direction of big pore size. These systematic differences indicate a correlation between the expected functional size of the channel (i.e., open and closed) and the projected diameter of the channel lumens in the crystalline arrays. These results suggest that it may be possible to lock or trap the arrays into one or another structural state using effectors, perhaps with longer incubations than used in these experiments (60 min).

In a previous report of the effects of the polyanionic modulator on membrane arrays of the VDAC channel, difference images were formed between correlation averages of control and +polyanion oblique arrays to infer the location of the polyanion (10). However, the simple approach used to form difference images in the earlier study is inadequate in light of the current results. For such comparisons to be valid, they must be made between control and +effector image averages within the same class (I, II, or III), otherwise difference images will reflect interclass variations as well as variations that might arise from the presence of a component not pres-

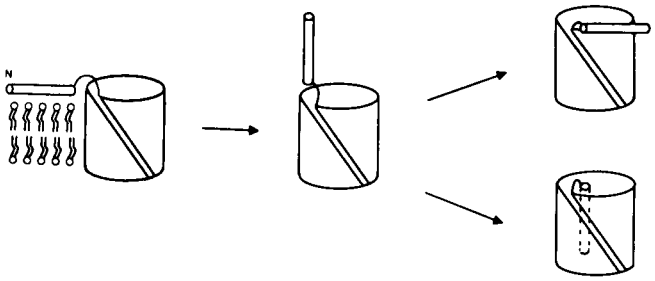

FIGURE 7 Hypothetical mechanism (35) by which the observed decrease in size of the VDAC pore may be explained by movement of a flexible arm from the bilayer to the lumen, which may be formed by a β-barrel (see discussion in references 35 and 37).

ent in the controls. More recently, difference images (not shown) have been computed between +polyanion array averages and control averages within class II; these indicate no statistically significant variations between the arrays. Therefore, the tentative localization of the polyanion on the VDAC array in reference 10 is incorrect. This raises the question of the nature of the extra density observed in the class II array averages at the corners of the unit cell. This region of the array recently has been identified as the site of binding of amphiphilic polypeptides (33) and so may also bind the amphiphilic polyanion, accounting for the extra density in this region. The fact that some control VDAC arrays also have extra density at this site suggests that endogenous mitochondrial components may be bound there in some preparations. Candidates for such components include cytochrome c, which has been shown to bind at this location on the VDAC array (34), and an endogenous protein "modulator" that exerts similar effects on VDAC's voltage dependence as does the polyanion (5).

Correlation between pore size and the presence of arms

The projected diameter of VDAC's pore decreases from 2.2 to 1.4 nm between cluster averages I and III. It is remarkable that this change in size is not associated with a change in packing of the channels, as expected for a major conformational change in the protein. One mechanism by which VDAC's pore diameter might significantly decrease without a major rearrangement of lumen structure would be by movement of an external part of the protein into the lumen (35). Interestingly, the change from large to small pore size along factor axis 1 correlates with the disappearance of the dense arms that extend laterally between the channels in class III and frozen-hydrated images. There is evidence that these arms represent amphiphilic α-helices formed by the NH_2-terminal segment of each VDAC polypeptide (36). It may be (as diagrammed in Fig. 7) that the arms detach from the bilayer under certain conditions and fall back on or into the channel lumen, giving rise to the class I image that has smaller pores than class III and no arms at the corners of the unit cell.

We thank Drs. Joachim Frank, Terence Wagenknecht, Tara Das, and Walter Gibson for helpful discussions in the course of this work. The technical assistance of Bernard Cognon, Hui Chen, and Shangmin Yan in collecting and processing some of the images used in the present analysis is gratefully acknowledged.

This study was supported by a research grant from the National Science Foundation (DMB-8916315) and by instrumentation grants from the National Science Foundation (PCM-8313045 and BBS-8721474) and the National Institutes of Health (1S10-RR-03998).

Received for publication 2 January 1992 and in final form 14 April 1992.

REFERENCES

1. Colombini, M. 1979. A candidate for the permeability pathway of the outer mitochondrial membrane. *Nature (Lond.).* 279:643–645.
2. Colombini, M. 1989. Voltage gating in the mitochondrial channel, VDAC. *J. Membr. Biol.* 111:103–111.
3. Benz, R. 1985. Porin from bacterial and mitochondrial outer membranes. *CRC Crit. Rev. Biochem.* 19:145–190.
4. Colombini, M., C. L., Yeung, J. Tung, and T. König. 1987. The mitochondrial outer membrane channel, VDAC, is regulated by a synthetic polyanion. *Biochim. Biophys. Acta.* 905:279–286.
5. Holden, M. J., and M. Colombini. 1988. The mitochondrial outer membrane channel, VDAC, is modulated by a soluble protein. *FEBS (Fed. Eur. Biochem. Soc.) Lett.* 241:105–109.
6. Benz, R., L. Wojtczak, W. Bosch, and D. Brdiczka. 1988. Inhibition of adenine nucleotide transport through the mitochondrial porin by a synthetic polyanion. *FEBS (Fed. Eur. Biochem. Soc.) Lett.* 231:75–80.
7. Mannella, C. A. 1984. Phospholipase-induced crystallization of channels in mitochondrial outer membranes. *Science (Wash. DC)* 224:165–166.
8. Mannella, C. A. 1986. Mitochondrial outer membrane channel (VDAC, Porin) two-dimensional crystals from neurospora. *In* Methods in Enzymology. S. Fleischer, and B. Fleischer, editors. Academic Press, London. 595–610.
9. Mannella, C. A., A. Ribeiro, and J. Frank. 1986. Structure of the channels in the outer mitochondrial membrane. *Biophys. J.* 49:307–318.
10. Mannella, C. A., and X. W. Guo. 1990. Interaction between the VDAC channel and a polyanionic effector. An electron microscopic study. *Biophys. J.* 57:23–31.
11. Thomas, L., E. Kocsis, M. Colombini, E. Erbe, B. L. Trus, and A. C. Steven. 1991. Surface topography and molecular stoichiometry of the mitochondrial channel, VDAC, in crystalline arrays. *J. Struct. Biol.* 106:161–171.
12. Mannella, C. A., X. W. Guo, and B. Cognon. 1989. Diameter of the mitochondrial outer membrane channel: evidence from electron microscopy of frozen-hydrated membrane crystals. *FEBS (Fed. Eur. Biochem. Soc.) Lett.* 253:231–234.
13. Guo, X. W. 1990. Cryo-electron microscopy and correlation averaging of frozen-hydrated, polymorphic 2D crystals of the mitochondrial outer membrane channel. *In* Proceedings of the XIIth International Congress for Electron Microscopy. L. D. Peachey and D. B. Williams, editors. San Francisco Press, San Francisco. 100–101.
14. Mannella, C. A. 1987. Electron microscopy and image analysis of the mitochondrial outer membrane channel, VDAC. *J. Bioenerg. Biomembr.* 19:329–340.

15. Colombini, M. 1987. Regulation of the mitochondrial outer membrane channel, VDAC. *J. Bioenerg. Biomembr.* 19:309–320.
16. Dill, E. T., M. J. Holden, and M. Colombini. 1987. Voltage gating in VDAC is markedly inhibited by micromolar quantities of aluminum. *J. Membr. Biol.* 99:187–196.
17. Mannella, C. A., M. Radermacher, and J. Frank. 1984. Three-dimensional structure of mitochondrial outer-membrane channels from fungus and liver. *In* Proceedings of the 42nd Annual Meeting of the Electron Microscopy Society of America. G. W. Bailey, editor. San Francisco Press, San Francisco. 644–645.
18. Engel, A., A. Massalski, H. Schindler, D. L. Dorset, and J. P. Rosenbusch. 1985. Porin channel triplets merge into single outlets in *Escherichia coli* outer membranes. *Nature (Lond.).* 317:643–645.
19. Mannella, C. A., and J. Frank. 1984. Negative staining characteristics of arrays of mitochondrial pore protein: use of correspondence analysis to classify different staining patterns. *Ultramicroscopy.* 13:93–102.
20. Guo, X. W. 1991. Electron microscopic studies of 2D membrane crystals of mitochondrial channel, VDAC, Ph.D. thesis. State University of New York at Albany. 131 pp.
21. Kuhlbrandt, W. 1982. Discrimination of protein and nucleic acids by electron microscopy using contrast variation. *Ultramicroscopy.* 7:221–232.
22. Mannella, C. A. 1982. Structure of the outer mitochondrial membrane: ordered arrays of porelike subunits in outer-membrane fractions from *Neurospora crassa* mitochondria. *J. Cell Biol.* 94:680–687.
23. Frank, J., B. Shimkin, and H. Dowse. 1981. Spider-a modular software system for electron image processing. *Ultramicroscopy.* 6:343–358.
24. Goldfarb, W., J. Frank, M. Kessel, J. C. Jsung, C. H. Kim, and T. E. King. 1979. Cytochrome oxidase vesicles with two-dimensional order. *In* Cytochrome Oxidase. T. E. King, Y. Orii, B. Chance, and K. Okunuki, editors. Elsevier North-Holland Biomedical Press, Amsterdam. 161–175.
25. Saxton, W. O. 1980. Matching and averaging over fragmented lattices. *In* Electron Microscopy at Molecular Dimensions. W. Baumeister and W. Vogell, editors. Springer-Verlag GmbH and Co., Berlin. 244–255.
26. Frank, J. 1982. New methods for averaging non-periodic objects and distorted crystals in biologic electron microscopy. *Optik.* 63:67–89.
27. Kessel, M., M. Radermacher, and J. Frank. 1984. The structure of the stalk surface layer of a brine pond microorganism: correlation averaging applied to a double layered structure. *J. Microsc. (Oxf.).* 139:63–74.
28. Saxton, W. O., and W. Baumeister. 1982. The correlation averaging of a regularly arranged bacterial cell envelope protein. *J. Microsc. (Oxf.).* 127:127–138.
29. Frank, J., W. Goldfarb, D. Eisenberg, and T. S. Baker. 1978. Reconstruction of glutamine synthetase using computer averaging. *Ultramicroscopy.* 3:283–290.
30. Frank, J., A. Verschoor, and M. Boublik. 1982. Multivariate statistical analysis of ribosome electron micrographs. L and R lateral views of the 40S subunit from HeLa cells. *J. Mol. Biol.* 161:107–137.
31. Unser, M., B. L. Trus, and A. C. Steven. 1989. Normalization procedures and factorial representations for classification of correlation-aligned images: a comparative study. *Ultramicroscopy.* 30:299–310.
32. Rachel, R., U. Jakubowski, H. Tietz, R. Hegrl, and W. Baumeister. 1986. Projected structure of the surface protein of *Deinococcus* radiodurans determined to 8 A resolution by cryomicroscopy. *Ultramicroscopy.* 20:305–316.
33. Mannella, C. A., X. W. Guo, and J. Dias. 1992. Binding of a synthetic targeting peptide to a mitochondrial channel protein. *J. Bioenerg. Biomembr.* 24:55–61.
34. Mannella, C. A., A. J. Ribeiro, and J. Frank. 1987. Cytochrome *c* binds to lipid domains in arrays of mitochondrial outer membrane channels. *Biophys. J.* 51:221–226.
35. Mannella, C. A. 1990. Structural analysis of mitochondrial pores. *Experientia (Basel).* 46:137–145.
36. Mannella, C. A., S. Stanley, D. D'Arcangelis, and J. A. Dias. 1992. Location of the N-terminus of the channel protein, VDAC, in the outer membrane of *Neurospora mitochondria. Biophys. J.* 61:A14. (Abstr.)
37. Mannella, C. A., M. Forte, and M. Colombini. 1992. Toward the molecular structure of the mitochondrial channel, VDAC. *J. Bioenerg. Biomembr.* 24:7–19.